Progress In Electromagnetics Research, PIER 99, 89–108, 2009

EXTENDED EXACT TRANSFER FUNCTION ALGORITHM FOR BISTATIC SAR OF TRANSLATIONAL INVARIANT CASE

J. P. Sun and S. Y. Mao

School of Electronic and Information Engineering
Beihang University
Beijing, China

G. H. Wang

School of Electrical and Electronic Engineering
Nanyang Technological University
Singapore

W. Hong

National Key Lab of MW Imaging Technology
Institute of Electronics, CAS
Beijing, China

Abstract—This paper presents an Extended Exact Transfer Function (EETF) algorithm for Bistatic Synthetic Aperture Radar (BiSAR) imaging of a Translational Invariant (TI) case. This algorithm adopts directly the 2D transfer function of monostatic SAR (MoSAR), instead of deriving a new one, by converting the BiSAR into an equivalent MoSAR. A new azimuth phase compensation function is constructed through exploiting this equivalency. Geometry distortion correction for BiSAR imaging result is considered in the proposed algorithm. In addition, the applying condition of the algorithm is also discussed. One desirable property of the proposed algorithm is that the computing flow and efficiency are the same as ETF algorithm for MoSAR. The effectiveness is validated by point target simulations with Tandem and forward-looking configuration.

Corresponding author: G. H. Wang (wang0330@ntu.edu.sg).

1. INTRODUCTION

Bistatic Synthetic Aperture Radar (BiSAR) obtains more flexible imaging geometry configuration than conventional monostatic SAR (MoSAR) because of spatial separation of transmitter and receiver. Bistatic geometry can possibly contribute to various SAR functions such as passive imaging and reconnaissance, forward-looking imaging, interferometric imaging, moving target indication, etc. [1–4]. So far, some research institutes have carried out experiments [5–9]. The imaging algorithm for BiSAR is different from the algorithms for Mo SAR due to the separation of transmitter and receiver. Time-domain Back-Projection (BP) algorithm is the most popular one in current practical applications [4, 5, 10] despite its inefficiency in computation. Literature [11] presents an approximate model in 2D frequency domain for the echoes of BiSAR with an arbitrary geometry configuration. Based on the approximate formula, Omega-K algorithm and 2D Inverse Scaled Fast Furior Transform (ISFFT) algorithm are proposed under different approximate conditions [12, 13]. In [14] and [15], other two Omega-K algorithms are proposed, respectively. Besides the algorithms mentioned above, there are some other BiSAR imaging algorithms, for example, equivalent monostatic imaging algorithm [16], Non-Linear Chirp Scaling Algorithm (NLCSA) [17], 'NuSAR' method [18, 19], Polar Formation Algorithm (PFA) [20], and the methods based on two-dimensional spectrum model [21, 22], etc.. The imaging algorithm for bistatic SAR is still in its infancy compared with the conventional imaging algorithm for MoSAR [4].

In BiSAR with Translational Invariant (TI) configuration, the transmitter is moving at the same direction and velocity as the receiver. The raw data point responses are sufficiently azimuth invariant within a processing block. TI imaging configuration, as used in many experiments of BiSAR at present [5–7], is suitable to produce large area stripmap images. Most of the algorithms mentioned above can be applied in TI configuration, however, with the shortcoming of large computational load. For example, the Stolt interpolation [12, 14, 15] or computation of transfer function by numerical method [18, 19] is required beforehand. With respect to TI configuration, an equivalent monostatic imaging algorithm is proposed firstly in [16]. It firstly transforms the BiSAR echo data into equivalent MoSAR data by SMILE transformation and then processes the transformed data through standard MoSAR imaging algorithm. Although the algorithm only aims at simple Tandem configuration, it can process data of BiSAR with only a few modifications on existing imaging processor for MoSAR. Thus, this algorithm has certain value in practice.

This paper presents a new equivalent monostatic imaging algorithm for BiSAR with TI configuration. The 'equivalent' here means that we do not derive a new 2D transfer function for BiSAR; instead, we use the given 2D transfer function of MoSAR directly. By introducing a virtual point target in the equivalent monostatic geometry, the phase history of BiSAR echo is approximated. Then we can get the new azimuth phase compensation function through a mapping between slant range and ground range determined by the bistatic imaging geometry; thus the focusing imaging for BiSAR of TI configuration along azimuth can be fulfilled. Meanwhile, the geometry distortion correction is also considered in the imaging process, which facilitates the post processing and BiSAR image understanding. As the imaging processing based on accurate 2D transfer function in MoSAR is named as Exact Transform Function (ETF) algorithm, we denote the imaging algorithm for BiSAR presented in this paper as Extended ETF (EETF) algorithm. The new algorithm maintains the advantages of conventional ETF algorithm in monostatic SAR, such as simple computing flow and high efficiency. The algorithm can be easily applied to BiSAR imaging with most TI configurations on existing MoSAR imaging processor.

The reminder of this paper is organized as follows. In Section 2, the equivalent monostatic imaging model for BiSAR system with TI configuration will be derived by investigating phase history of BiSAR echo. In Section 3, the EETF algorithm for BiSAR imaging will be developed by introducing virtual point targets. Furthermore, the applying condition of the algorithm will also be discussed. In Section 4, we will validate the effectiveness of this algorithm by point target simulations for two typical TI BiSAR cases. The conclusions will be finally summarized in Section 5.

2. EQUIVALENT MONOSTATIC IMAGING MODEL FOR BISAR

In this section, we will develop a new method that transforms the bistatic configuration to an equivalent monostatic one. The equivalence is achieved by making the constant term, the linear term and the quadratic term of the true bistatic range history equal to their counterparts of an equivalent monostatic range history.

The imaging geometry for stripmap mode BiSAR of TI configuration is shown in Fig. 1. Transmitter S_1 and receiver S_2 are carried on moving platforms with same velocity of v, and altitudes of h_1 and h_2, respectively. Let t be the azimuth time. When $t = 0$, the instant slant range between the swath centre O and antenna phase

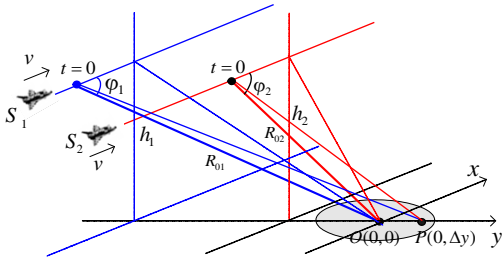

Figure 1. Imaging geometry for stripmap mode BiSAR with TI configuration.

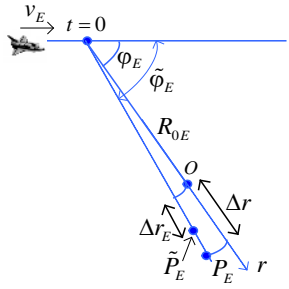

Figure 2. Imaging geometry of equivalent monostatic SAR.

center is R_{01} for transmitter and R_{02} for receiver. The squint angle, defined as the angle between the radar Light of Sight (LOS) and the flying direction, is φ_1 for transmitter and φ_2 for receiver, respectively.

According to the geometry shown in Fig. 1, the range history of signal from S_1 to S_2 via centre O can be written as

$$\begin{aligned} R(t) \;=\; & \sqrt{(R_{01}\sin\varphi_1)^2+(vt-R_{01}\cos\varphi_1)^2} \\ & +\sqrt{(R_{02}\sin\varphi_2)^2+(vt-R_{02}\cos\varphi_2)^2}. \end{aligned} \tag{1}$$

Suppose that the synthetic aperture length is far less than the distance between radar and target area, then we can apply Taylor expansion to (1) as bellow

$$\begin{aligned} R(t) \;\approx\; & (R_{01}+R_{02})-v(\cos\varphi_1+\cos\varphi_2)t+\frac{1}{2}v^2\left(\frac{\sin^2\varphi_1}{R_{01}}+\frac{\sin^2\varphi_2}{R_{02}}\right)t^2 \\ & +\frac{1}{2}v^3\left(\frac{\sin^2\varphi_1\cos\varphi_1}{R_{01}^2}+\frac{\sin^2\varphi_2\cos\varphi_2}{R_{02}^2}\right)t^3\cdots. \end{aligned} \tag{2}$$

To obtain equivalent monostatic model for BiSAR, the received BiSAR echo signal should be transformed into signal of MoSAR correspondingly. As this transformation is performed in echo domain, we consider the equivalent imaging geometry in the data collection plane. The equivalent imaging geometry is shown in Fig. 2, where v_E, φ_E, R_{0E} are equivalent platform velocity, equivalent squint angle and equivalent slant range, respectively.

According to Fig. 2, for equivalent monostatic system, the range history of echo signal returned from central point O is

$$\begin{aligned} & R_E(t) = 2\sqrt{(R_{0E}\sin\varphi_E)^2+(v_Et-R_{0E}\cos\varphi_E)^2} \\ & \approx 2R_{0E}-2v_E\cos\varphi_E+\frac{v_E^2\sin^2\varphi_E}{R_{0E}}t^2+\frac{v_E^3\sin^2\varphi_E\cos\varphi_E}{R_{0E}^2}t^3+\cdots. \end{aligned} \tag{3}$$

Generally, parameters in the equivalent system should be chosen to make $R_E(t)$ as close as possible to BiSAR range history in (1). Thus, we make the constant term, linear term (Doppler centroid) and quadratic term (Doppler rate) in (2) to be equal to the corresponding terms in (3). This is because these terms mainly affect focusing. Consequently, a system of equations with three unknowns, say, v_E, φ_E and R_{0E}, can be obtained. The solution of the system of equations can be achieved and the parameters of equivalent model are

$$\begin{aligned} R_{0E} &= \frac{R_{01}+R_{02}}{2} \\ v_E &= \frac{v}{2}\sqrt{\left(1+\frac{R_{02}}{R_{01}}\sin^2\varphi_1\right)+\left(1+\frac{R_{01}}{R_{02}}\sin^2\varphi_2\right)+2\cos\varphi_1\cos\varphi_2} \\ \varphi_E &= \cos^{-1}\left(\frac{v}{v_E}\cdot\frac{(\cos\varphi_1+\cos\varphi_2)}{2}\right). \end{aligned} \tag{4}$$

With the equivalent monostatic model determined by (4), fully focused image result can be achieved for point target at the position of swath centre by ignoring the equivalent range error from above quadratic terms. We also examine the effectiveness of focusing for point targets at other positions in the swath. The x-y coordinate of ground scene is shown is Fig. 1. For point target $P(0,\Delta y)$, the corresponding range history can be written as

$$\begin{aligned} R(t;\Delta y) &= R_1(t;\Delta y)+R_2(t;\Delta y) \\ R_1(t;\Delta y) &= \sqrt{(Y_{01}+\Delta y)^2+h_1^2+(vt-R_{01}\cos\varphi_1)^2} \\ R_2(t;\Delta y) &= \sqrt{(Y_{02}+\Delta y)^2+h_2^2+(vt-R_{02}\cos\varphi_2)^2} \\ Y_{01} &= \sqrt{(R_{01}\sin\varphi_1)^2-h_1^2}, Y_{02}=\sqrt{(R_{02}\sin\varphi_2)^2-h_2^2}\,. \end{aligned} \tag{5}$$

Then, the range at the moment of $t=0$ is

$$\begin{aligned} R(0;\Delta y) &= R_1(0;\Delta y)+R_2(0;\Delta y) \\ &= \sqrt{R_{01}^2+\Delta y^2+2Y_{01}\Delta y}+\sqrt{R_{02}^2+\Delta y^2+2Y_{02}\Delta y}\,. \end{aligned} \tag{6}$$

At this very moment, the difference between this range and the two-way slant range in the equivalent model determined by (4) is

$$\begin{aligned} 2\Delta r &= R(0;\Delta y)-2R_{0E} \\ &= R(0;\Delta y)-(R_{01}+R_{02}) \\ &= \sqrt{R_{01}^2+\Delta y^2+2Y_{01}\Delta y}+\sqrt{R_{02}^2+\Delta y^2+2Y_{02}\Delta y}-(R_{01}+R_{02})\,. \end{aligned} \tag{7}$$

Generally, the width of imaging region is far less than the range from the region to radar. That means $\Delta y << R_{01},\ \Delta y << R_{02}$. Therefore, Taylor expansion can be implemented to (7) with respect to Δy. The result after quadratic expansion is

$$\begin{aligned} 2\Delta r &\approx b \cdot \Delta y + a \cdot \Delta y^2, \\ b &= \frac{Y_{01}}{R_{01}} + \frac{Y_{02}}{R_{02}}, \\ a &= \frac{1}{2}\left\{ \frac{1}{R_{01}}\left(1 - \frac{Y_{01}^2}{R_{01}^2}\right) + \frac{1}{R_{02}}\left(1 - \frac{Y_{02}^2}{R_{02}^2}\right)\right\}. \end{aligned} \tag{8}$$

The formula above is a quadratic equation with respect to Δy and the effective solution can be obtained as

$$\Delta y = \begin{cases} \frac{\sqrt{b^2+8a\Delta r}-b}{2a} & a \neq 0 \\ \frac{2\Delta r}{b} & a = 0 \end{cases}. \tag{9}$$

To ensure the solution in formula (9) to be real, the condition below must be satisfied

$$\Delta r \geq -\frac{b^2}{8a}. \tag{10}$$

Although formula (8) is an approximate equation, the solution expressed in (9) is still meaningful. As for the slant range r corresponding to some range bin in raw data domain, the ground range position Δy corresponding to the slant range $\Delta r = r - R_{0E}$ can be calculated. Then we can obtain range history and echo signal numerically using imaging geometry parameters. Consequently, formula (9) can be applied in 'NuSAR' method introduced in [18, 19]. Meanwhile, formula (9) can also be used to accomplish the geometry distortion correction in range direction. We will discuss this point in the next section.

From the linear term of Taylor expansion of $R(t; \Delta y)$, we can obtain the Doppler centroid of point target P, which is different from the Doppler centroid of centre O with equivalent squint angle φ_E. The new equivalent squint angle for point target P in equivalent monostatic model shown in Fig. 2 can be calculated as

$$\tilde{\varphi}_E = \cos^{-1}\left(\frac{v}{2v_E}\left(\frac{R_{01}\cos\varphi_1}{R_1(0;\Delta y)} + \frac{R_{02}\cos\varphi_2}{R_2(0;\Delta y)}\right)\right). \tag{11}$$

A virtual point target P_E in equivalent monostatic model corresponding to point P can be defined by Δr and $\tilde{\varphi}_E$, both of which are determined by Δy. The slant range and Doppler centroid of the echo returned from the virtual target in monostatic model are the same as

those from the point P in bistatic geometry, as shown in Fig. 2. The one-way range history of P_E in monostatic model is

$$R_E(t;\Delta r)=\sqrt{((R_{0E}+\Delta r)\cdot\sin\tilde{\varphi}_E)^2+(v_E t-(R_{0E}+\Delta r)\cdot\cos\tilde{\varphi}_E)^2}. \quad (12)$$

When we apply the equivalent model for imaging, the virtual target P_E determined by (4) replaces target P in bistatic geometry, and the difference of range history in corresponding imaging geometry must satisfy focusing condition

$$|R_1(t;\Delta y)+R_2(t;\Delta y)-2R_E(t;\Delta r)|<\frac{\lambda}{8},\quad -\frac{T_a}{2}<t<\frac{T_a}{2} \quad (13)$$

where λ is the wavelength of radar system, T_a is synthetic aperture time. Inequality (13) indicates that the size of effectively focusing region is limited by equivalent parameters determined by (4) when we apply the equivalent monostatic model for imaging. This limitation is determined by imaging geometry and system parameters of BiSAR instead of the focusing performance of specific monostatic imaging algorithm. Though the analytical solution about Δy in (13) can be obtained theoretically, in practice the numerical approximation method can be used. That is to substitute different value of Δy into (5), (6), (11), (12) and examine whether inequality (13) is satisfied. The range in which Δy meets (13) is the size of effectively focusing region. In addition, Δy should satisfy the condition that makes sure Taylor expansion of (8) can be performed.

3. EXTENDED ETF ALGORITHM FOR BISAR IMAGING

The flow chart of conventional ETF algorithm for MoSAR imaging is shown in Fig. 3 [23–26]. The bulk range processing transfer function $H_s(f_a, f_r; r_{ref})$ is the conjugate version of the 2D exact transfer function, and is applied in the 2D spectral domain. It performs range compression, range cell migration correction (RCMC), secondary range compression (SRC), and the compensation of all higher-order phase terms for all points located at the reference range (preferably chosen to be in the swath center). $H_{\Delta\Phi}(f_a, r)$ is the azimuth phase compensation function. Due to the fact that there is no differential RCMC in ETF algorithm, the difference between range migration curves of point targets in imaging region should not exceed half range resolution unit. The effective imaging swath size will be limited for high resolution and the limitation needs to be overcome by means of block processing along range direction [25].

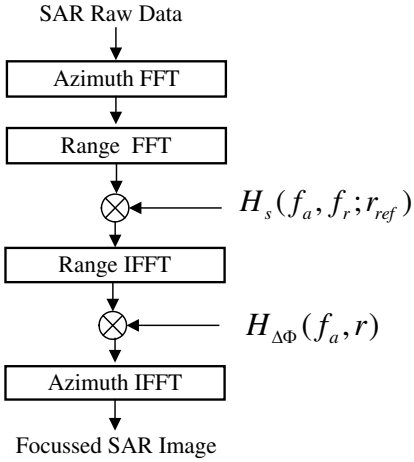

Figure 3. Flow diagram for the ETF algorithm.

When ignoring the restriction of (13), we can apply directly the conventional ETF algorithm to the equivalent monostatic model derived in Section 2 and denote this processing as EETF-1. The corresponding range and azimuth functions are to be derived as follows. Let the transmitting signal to be

$$s(\tau) = rect\left(\tau/T_p\right) \exp\left(j2\pi f_c \tau + j\pi\gamma\tau^2\right), \tag{14}$$

where τ is fast time, T_p the chirp signal with pulse width, f_c the center frequency, and γ the chirp rate. Let $r_{ref} = R_{0E}$. Then, the range processing transfer function is

$$H_s(f_a, f_r; R_{0E}) = C \cdot \exp\left\{j\frac{4\pi}{\lambda} \cdot R_{0E} \cdot \sin\varphi_E \cdot \sqrt{\left(1+\frac{f_r}{f_c}\right)^2 - \left(\frac{\lambda f_a}{2v_E}\right)^2}\right\}$$

$$\cdot \exp\left\{j\pi\frac{f_r^2}{\gamma}\right\} \cdot \exp\left\{-j4\pi \cdot R_{0E} \cdot \left(\frac{f_r}{c} - \frac{f_a}{v_E}\cos\varphi_E\right)\right\}, \tag{15}$$

where f_a is the azimuth frequency with respect to slow time t, while f_r is the range frequency with respect to fast time τ. The azimuth phase compensation function is:

$$H_{\Delta\Phi,\mathrm{EETF}-1}(f_a, r) = \exp\left\{\frac{4\pi}{\lambda}(r - R_{0E}) \cdot \sin\varphi_E \cdot \sqrt{1\left(\frac{\lambda f_a}{2v_E}\right)^2}\right\}. \tag{16}$$

According to the illustrations in Fig. 3, the implementation of EETF-1 algorithm is briefly introduced as follows. We firstly implement (15)

in 2D frequency domain to accomplish range compression together with RCMC for all targets by IFFT along range direction. Then we perform the successive step of phase error compensation in Range-Doppler domain using (16). Finally azimuth compression is carried out through IFFT along azimuth direction. Details about this process, as well as derivations of (15) and (16), is available in many literatures on MoSAR imaging [23–27].

As (13) indicates, the effective imaging swath size will be limited by bistatic imaging geometry if we simply use EETF-1 algorithm mentioned above. We therefore propose a new algorithm to overcome this limitation.

For virtual target P_E in equivalent monostatic model and target P in real bistatic geometry, the difference of range history between them is

$$\Delta R(t) = R_1(t;\Delta y) + R_2(t;\Delta y) - 2R_E(t;\Delta r). \tag{17}$$

According to the definition of virtual target P_E, there remain only quadratic and higher order terms after Taylor expansion on $\Delta R(t)$ as shown below:

$$\Delta R(t) \approx \left\{ \frac{v^2}{2} \left(\frac{R_1^2(0;\Delta y) - R_{01}^2 \cos^2\varphi_1}{R_1^3(0;\Delta y)} + \frac{R_2^2(0;\Delta y) - R_{02}^2 \cos^2\varphi_2}{R_2^3(0;\Delta y)} \right) - \frac{v_E^2 \sin^2\tilde{\varphi}_E}{R_{0E} + \Delta r} \right\} t^2 + \cdots . \tag{18}$$

There is no doubt that the effective imaging swath size will be expanded if we eliminate the quadratic term (corresponding to quadratic phase error along azimuth) sufficiently because this term is the major component of $\Delta R(t)$.

As shown in Fig. 2, for P_E, we introduce a new equivalent virtual point $\tilde{P}_E$ whose Doppler centroid is same as P_E and slant range difference with respect to centre is Δr_E. Suppose Δr_E makes the coefficient of quadratic term in (18) to be zero, then we can obtain Δr_E as

$$\Delta r_E = \frac{2v_E^2 \sin^2\tilde{\varphi}_E}{v^2} \left(\frac{R_1^2(0;\Delta y) - R_{01}^2 \cos^2\varphi_1}{R_1^3(0;\Delta y)} + \frac{R_2^2(0;\Delta y) - R_{02}^2 \cos^2\varphi_2}{R_2^3(0;\Delta y)} \right)^{-1} - R_{0E}. \tag{19}$$

In echo signal domain, $\tilde{P}_E$ in equivalent monostatic geometry has the same Doppler centroid and Doppler rate but different delay time compared with point P in real bistatic geometry. Suppose that the slant range of P in equivalent monostatic model is r, then the equivalent slant range of the new virtual point $\tilde{P}_E$ can be expressed as

a function of r as bellow

$$r_E(r) = R_{0E} + \Delta r_E(r). \tag{20}$$

The calculation of equivalent slant range r_E according to original slant range r is as follows. Firstly, we compute the slant range difference as $\Delta r = r - R_{0E}$ for each range bin in monostatic model. Secondly, substitute Δr in (9) to obtain Δy in real bistatic geometry. After that, we can determine Δr_E using (5), (6), (11) and (19). Finally, substitute it into (20) to get r_E.

In order to improve the effective size of imaging swath, the modification to EETF-1 algorithm can be simply implemented to azimuth compensation function. Specifically, we can apply the azimuth phase compensation function of the new virtual point $\tilde{P}_E$ to the azimuth signal in the slant range r of the origin point P. The azimuth phase compensation function after modification is shown as follows

$$H_{\Delta\Phi,\mathrm{EETF-2}}(f_a,r) = \exp\left\{\frac{4\pi}{\lambda}(r_E(r) - R_{0E}) \cdot \sin\varphi_E \cdot \sqrt{1 - \left(\frac{\lambda f_a}{2v_E}\right)^2}\right\}. \tag{21}$$

According to the result of (11), the equivalent squint angles of virtual point targets with respect to different slant ranges in monostatic model are different from each other. Consequently, EETF-1 algorithm incurs not only azimuth defocusing but also distortion of azimuth position. Correction of azimuth geometry distortion is a process of compensation on Doppler centroid. We firstly get equivalent squint angle $\tilde{\varphi}_E$ corresponding to different slant range r by using (9), (5), (6) and (11). Then, the Doppler centroid varying with respect to slant range in equivalent monostatic model can be written as

$$f_{dc}(r) = 2 \cdot \frac{v_E \cos\tilde{\varphi}_E(r)}{\lambda}. \tag{22}$$

Referring to the Doppler centroid on the reference range, the compensation function for correction of azimuth geometry distortion is

$$H_{Az,\mathrm{EETF-2}}(f_a, r) = \exp\left\{-j2\pi \frac{f_{dc}(r) - f_{dc}(r_E)}{f_{dr}(r_E)} f_a\right\}, \tag{23}$$

where the reference Doppler rate is

$$f_{dr}(r_E) = -2 \cdot \frac{v_E^2 \sin^2\tilde{\varphi}_E(r_E)}{\lambda r_E}. \tag{24}$$

We denote the imaging process using (15), (21) and (23) as EETF-2 algorithm.

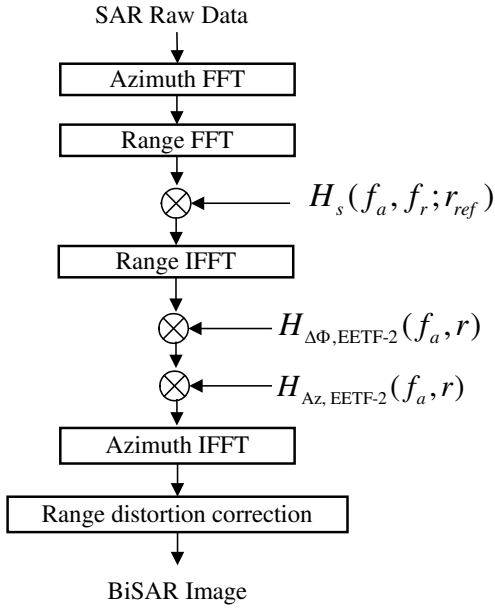

Figure 4. Flow diagram for the BiSAR EETF-2 algorithm.

Owing to the fact that the relation between Δy and Δr is not simply linear in common, the samples along y-axis are with non-uniform sampling intervals although samples along slant range r with equal intervals. Thus, there are obvious geometry distortions along range direction in imaging result after azimuth IFFT. The correction can be implemented through interpolation and resampling along range direction, while resample index is determined by (11). The complete processing flow diagram of new BiSAR EETF-2 algorithm is thus shown as Fig. 4.

The imaging swath size limitation of EETF-1 and EETF-2 algorithm is discussed as follows. Both of the two algorithms correct RCMC using transfer function $H_s(f_a, f_r; R_{0E})$ in 2D frequency domain without differential RCMC, which means the difference between range migration curves of point targets in imaging region can not exceed half range resolution unit. That is

$$\left| \begin{array}{l} \sqrt{(R_{0E}+\Delta r)^2 \sin^2\varphi_E + (v_E t - (R_{0E}+\Delta r)\cos\varphi_E)^2} \\ -\sqrt{R_{0E}^2 \sin^2\varphi_E + (v_E t - R_{0E}\cos\varphi_E)^2} - \Delta r \end{array} \right| < \frac{\rho_r}{2},$$
$$-\frac{T_a}{2} < t < -\frac{T_a}{2}, \tag{25}$$

where ρ_r is the range resolution. As for EETF-2, it must satisfy the basic condition of effective range transform described as (10) and the condition using Taylor expansion in (8) and (18), besides the condition imposed by (25). While for EETF-1, the main limitation is from formula (13) in addition to all limitations mentioned above.

4. SIMULATION EXPERIMENTS

To validate the effectiveness of the proposed algorithm, we select two typical BiSAR geometry of TI configuration. The parameters of radar system used in simulations are shown in Table 1. We also assume that in the process of data collecting, the synthetic aperture length meets the requirement of 0.5 m theoretic azimuth resolution for BiSAR.

In the imaging geometry defined as Fig. 1, we locate three point targets with coordinate in x-y coordinate system on ground $P_1(0, -500\,\mathrm{m})$, $P_2(0, 0)$ and $P_3(0, 500\,\mathrm{m})$, respectively.

We firstly investigate a typical Tandem configuration (S_R has same flight path as S_T) as shown in Fig. 5. The geometry parameters of platforms are: $h_1 = h_2 = 4000\,\mathrm{m}$, $\varphi_1 = 110^\circ$, $\varphi_2 = 60^\circ$, $R_{OR} = 8513\,\mathrm{m}$,

Table 1. Radar system parameters for simulation.

Parameter	Value
Center frequency	10 GHz
Chirp bandwidth	150 MHz
ADC sampling rates	200 MHz
Pulse duration	5 μs
Platform velocity	100 m/s
PRF	600 Hz

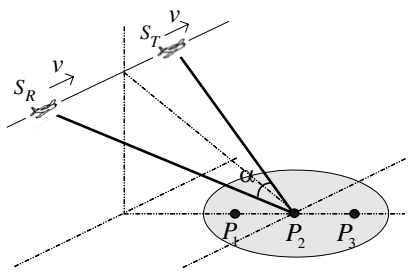

Figure 5. The illumination geometry for simulation Tandem configuration.

$R_{OT} = 9238\,\text{m}$. The imaging geometry has a large bistatic angle $\alpha = 50°$. Fig. 6 shows the BiSAR imaging result of EETF-1 and of EETF-2 before and after range geometry correction. As we can see in the figure, ideal focusing is achieved for central point target P_2 at reference slant range in both results. But for boundary points P_1 and P_3, the result of EETF-1 shows obvious defocusing and geometry distortions. Solving (13) using the system parameters mentioned above, we can obtain the effective foucusing region $-50.41\,\text{m} < y < 51.38\,\text{m}$ for EETF-1. Both

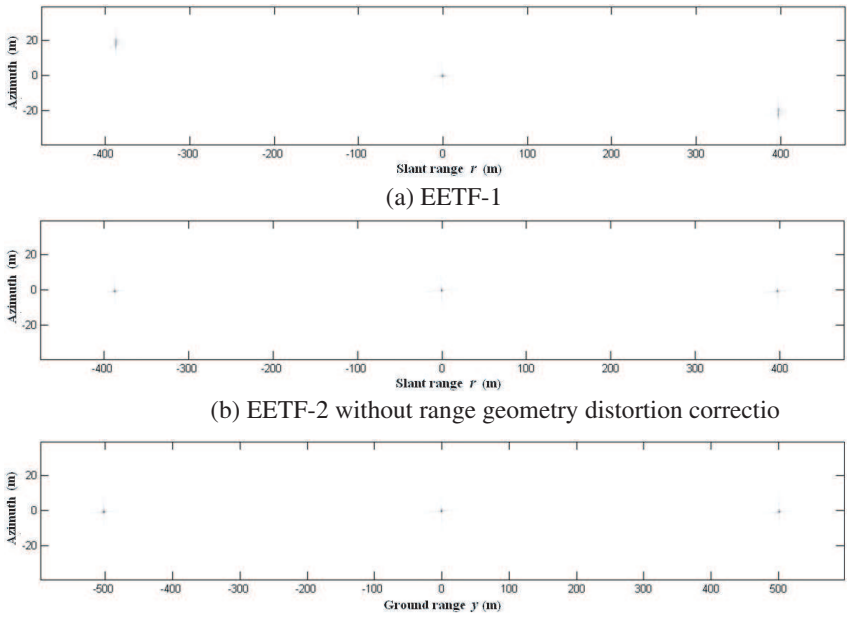

(a) EETF-1

(b) EETF-2 without range geometry distortion correctio

(c) EETF-2 with range geometry distortion correction

Figure 6. BiSAR images from different methods for Tandem configuration.

Table 2. Imaging qualities of point targets from EETF-2 for Tandem configuration.

	azimuth			range		
	ρ_a (m)	PSLR (dB)	ISLR (dB)	ρ_r(m)	PSLR (dB)	ISLR (dB)
P_1	0.51	−12.09	−8.26	1.00	−12.15	−8.96
P_2	0.50	−13.13	−9.84	1.00	−13.25	−9.78
P_3	0.50	−12.23	−8.31	1.00	−12.27	−8.89

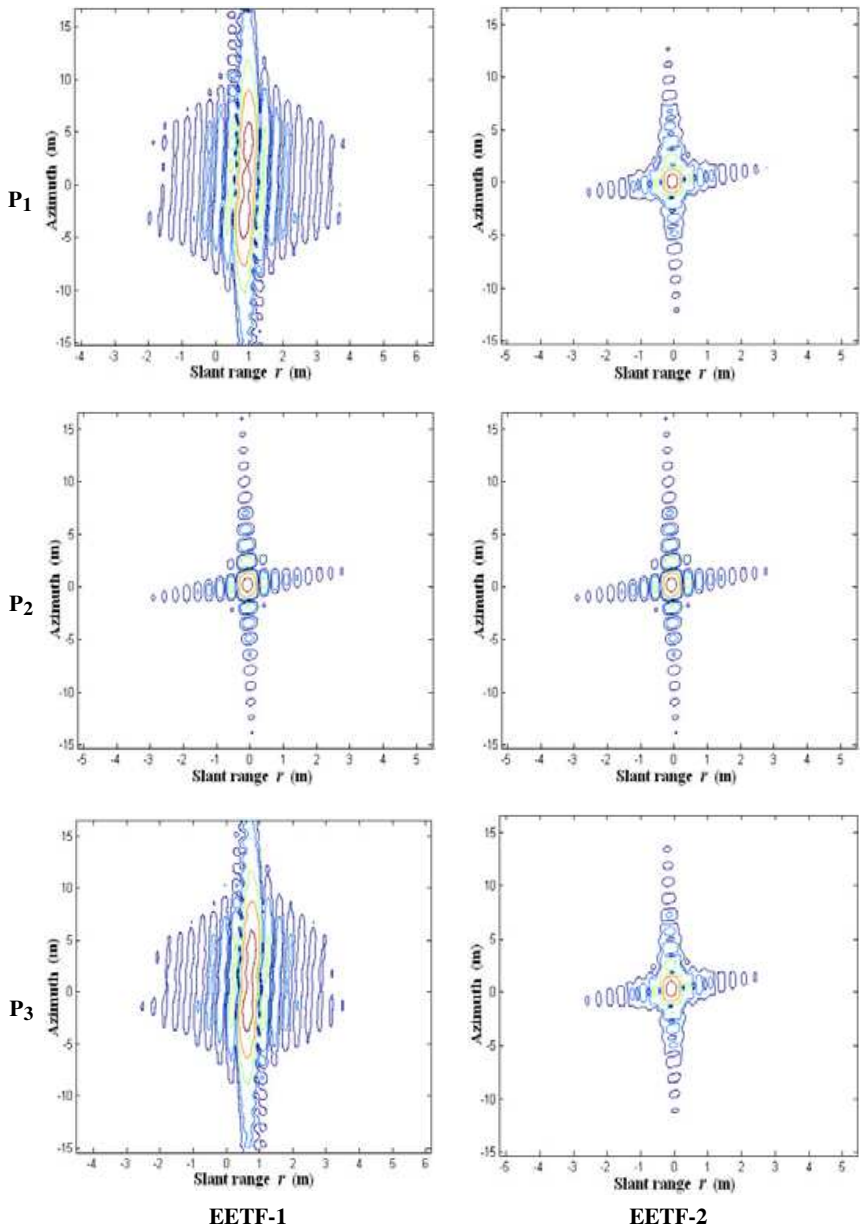

Figure 7. Point target responses from different methods for Tandem configuration.

the simulation and analytical results validate the swath size limitation of focusing imaging for EETF-1. Fig. 6(c) indicates that the result of (9) is accurate enough to range geometry distortion correction. The point target responses obtained from EETF-1 and EETF-2 are compared in Fig. 7. The imaging qualities of the three targets from EETF-2 are shown in Table 2, which shows that the focusing quality

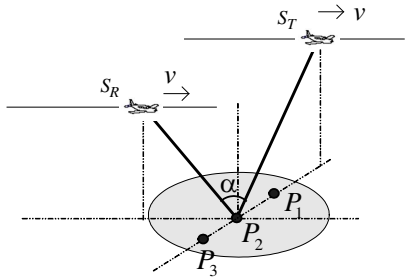

Figure 8. Illumination geometry for simulation forward-looking configuration.

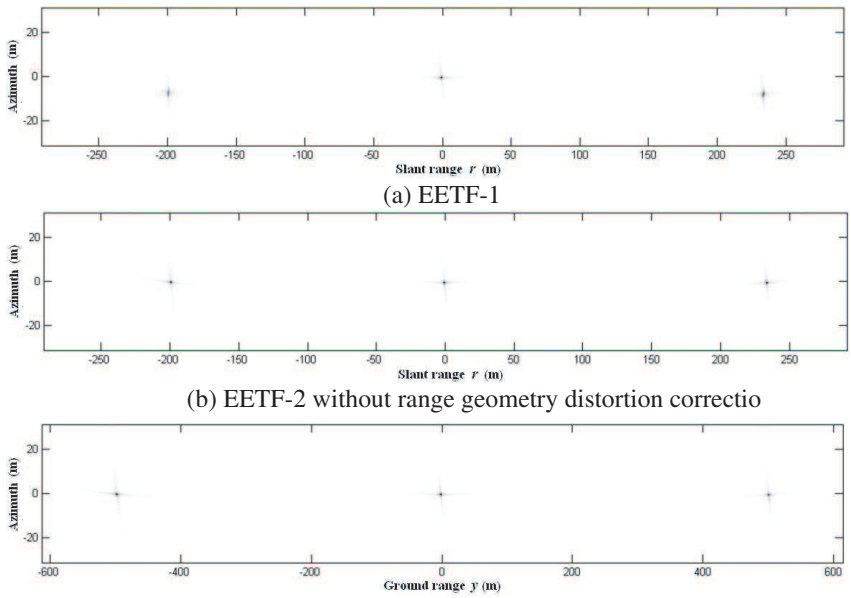

(a) EETF-1

(b) EETF-2 without range geometry distortion correctio

(c) EETF-2 with range geometry distortion correction

Figure 9. BiSAR images from different methods for forward-looking configuration.

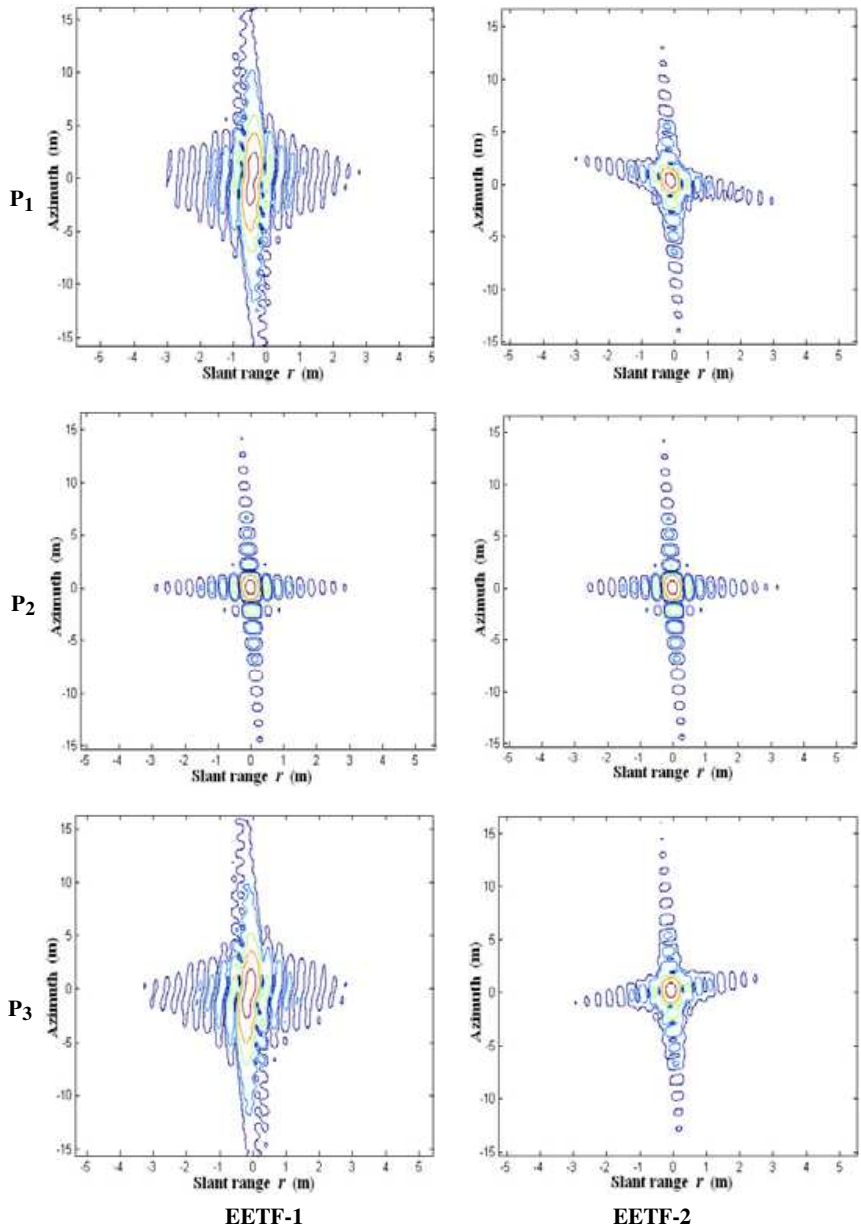

Figure 10. Point target responses from different methods for forward-looking configuration.

Table 3. Imaging qualities of point targets from EETF-2 for forward-looking configuration.

	azimuth			range		
	ρ_a (m)	PSLR (dB)	ISLR (dB)	ρ_r (m)	PSLR (dB)	ISLR (dB)
P_1	0.52	−11.97	−8.05	1.00	−12.06	−8.35
P_2	0.50	−13.11	−9.85	1.00	−13.20	−9.78
P_3	0.51	−12.15	−8.28	1.00	−12.17	−8.59

of two boundary points is satisfactory.

Secondly, we study a special TI configuration. As the fact that the azimuth resolution of BiSAR is determined by the imaging geometry configurated by transmitter and receiver, the forward-looking mode is applicable (It is well known that for monostatic SAR, the azimuth resolution capacity cannot be obtained for forward-looking mode). We denote this imaging geometry for BiSAR as forward-looking configuration. As shown in Fig. 8, the transmitter is working on side looking mode while the receiver is working on forward-looking mode. The parameters of platforms are: $h_1 = h_2 = 4000\,\text{m}$, $\varphi_1 = 90°$, $\varphi_2 = 70°$, $R_{OR} = 8000\,\text{m}$, $R_{OT} = h_2/\cos(\varphi_2) = 4257\,\text{m}$. The imaging geometry is corresponding to a bistatic angle $\alpha = 62°$.

For forward-looking mode, Fig. 9 shows the BiSAR imaging result of EETF-1 and of EETF-2 before and after range geometry correction. Like the Tandem mode, ideal focusing is achieved for central point target P_2 at reference slant range in both results. But for boundary points P_1 and P_3, the result of EETF-1 shows obvious defocusing and geometry distortions. The point target responses processed by EETF-1 and EETF-2 are compared in Fig. 10. The quality of imaging of the three targets using EETF-2 is shown in Table 3 and the focusing quality of two boundary points also is satisfactory.

To further evaluate the effectiveness of the proposed EETF-2 algorithm, we can compare the results of this paper with ideal focusing results from Back-Projection algorithm. Particularly, from Back-projection algorithm, the ideal focusing result has PLSR $\approx -13.3\,\text{dB}$, ISLR $\approx -9.8\,\text{dB}$. Comparing the EETF-2 results of this paper with the ideal ones, the IRW (Impulse Response Width) broadening is less than 5%; PLSR rising is less than 2 dB; and ISLR rising is less than 3 dB. Thus, the proposed algorithm can well meet the requirement of moderate focusing accuracy [27].

5. CONCLUSIONS

This paper presents a new equivalent monostatic imaging method for BiSAR with TI configuration. Unlike most literatures about BiSAR imaging algorithm, the conventional 2D transfer function of monostatic SAR is applied directly to BiSAR imaging processing. The phase history of BiSAR echo is approximated by introducing virtual point targets in the equivalent monostatic geometry. The new azimuth phase compensation function is obtained based on the mapping between ground range and slant range in bistatic imaging geometry. In the new EETF-2 algorithm, geometry distortion correction of BiSAR imaging result was also considered. Through point target simulations of typical Tandem configuration and forward-looking configuration, the effectiveness of the algorithm was validated. Compared with some new and accurate bistatic SAR imaging algorithms (e.g., NuSAR in [18, 19]), EETF-2 algorithm has the same computing flow and efficiency as ETF algorithm for conventional monostatic SAR (inherits some desirable properties of conventional ETF algorithm such as simple computation flow and high computation efficiency. Consequently, the algorithm can be easily implemented by few improvements on existing monostatic SAR imaging processor for most bistatic SAR in TI mode.

REFERENCES

1. Ben Kassem, M. J., J. Saillard, and A. Khenchaf, "BISAR mapping I. Theory and modeling," *Progress In Electromagnetics Research*, PIER 61, 39–65, 2006.
2. Ben Kassem, M. J., J. Saillard, and A. Khenchaf, "BISAR mapping II. Treatment, simulation and experimentation," *Progress In Electromagnetics Research*, PIER 61, 67–87, 2006.
3. Krieger, G. and A. Moreira, "Spaceborne bi- and multistatic SAR: Potentials and challenges," *IEE Proc. Radar Sonar Navig.*, Vol. 153, No. 3, 184–198, 2006.
4. Ender, J., "A step to bistatic SAR processing," *Proc. of EUSAR*, 356–359, 2004.
5. Ender, J., I. Walterscheid, and A. Brenner, "New aspects of bistatic SAR: Processing and experiments," *Proc. of IGARSS*, 1758–1762, 2004.
6. Walterscheid, I., J. Ender, A. Brenner, and O. Loffeld, "Bistatic SAR processing and experiments," *IEEE Trans. Geosci. Remote Sens.*, Vol. 44, No. 10, 2710–2717, 2006.
7. Dubois-Fernandez, P., H. Cantalloube, B. Vaizan, G. Krieger,

R. Horn, M. Wendler, and V. Giroux, "ONERA-DLR bistatic SAR campaign: Planning, data acquisition, and first analysis of bistatic scattering behaviour of natural and urban targets," *IEE Proc. Radar Sonar Navig.*, Vol. 153, No. 3, 214–223, 2006.

8. Yates, G, A. M. Horne, A. P. Blake, R. Middleton, and D. B. Andre, "Bistatic SAR image formation," *IEE Proc. Radar Sonar Navig.*, Vol. 153, No. 3, 208–213, 2006.
9. Marcos, J., P. Dekker, J. Mallorqui, A. Aguasca, and P. Prats, "SABRINA: A SAR bistatic receiver for interferometric application," *IEEE Trans. Geosci. Remote Sens. Lett.*, Vol. 4, No. 2, 307–311, 2007.
10. Ding, Y. and D. C. Munson, Jr., "A fast back-projection algorithm for bistatic SAR imaging," *IEEE International Conference on Image Processing*, Vol. 2, 449–452, 2002.
11. Loffeld, O., H. Nies, V. Peters, and S. Knedlik, "Models and useful relations for bistatic SAR," *IEEE Trans. Geosci. Remote Sens.*, Vol. 42, No. 10, 2031–2038, 2004.
12. Walterscheid, I., J. Ender, A. Brenner, and O. Loffeld, "Bistatic SAR processing using an omega-k type algorithm," *Proc. of IGARSS*, Vol. 2, 1064–1067, 2005.
13. Natroshvili, K., O. Loffeld, H. Nies, A. M. Ortiz, and S. Knedlik, "Focusing of general bistatic SAR configuration data with 2-D inverse scaled FFT," *IEEE Trans. Geosci. Remote Sens.*, Vol. 44, No. 10, 2718–2727, 2006.
14. Giroux, C., H. Cantalloube, and F. Daout, "An Omega-K algorithm for SAR bistatic systems," *Proc. of IGARSS*, Vol. 2, 1060–1063, 2005.
15. Qiu, X. L., D. H. Hu, and C. B. Ding, "An Omega-K algorithm with phase error compensation for bistatic SAR of a translational invariant case," *IEEE Trans. Geosci. Remote Sens.*, Vol. 46, No. 8, 2224–2232, 2008.
16. D'Aria, D., A. M. Guarnieri, and F. Rocca, "Focusing bistatic synthetic aperture radar using dip move out," *IEEE Trans. Geosci. Remote Sens.*, Vol. 42, No. 7, 1362–1376, 2004.
17. Wong, F. H. and T. S. Yeo, "New applications of nonlinear chirp scaling in SAR data processing," *IEEE Trans. Geosci. Remote Sens*, Vol. 39, No. 5, 946–953, 2001.
18. Bamler, R., F. Meyer, and W. Liebhar, "No math: Bistatic SAR processing using numerically computed transfer functions," *Proc. of IGARSS*, 1844–1847, 2006.
19. Bamler, R., F. Meyer, and W. Liebhart, "Processing of bistatic

SAR data from quasi-stationary configurations," *IEEE Trans. Geosci. Remote Sens.*, Vol. 45, No. 11, 3350–3358, 2007.

20. Rigling, B. D. and R. L. Moses, "Polar format algorithm for bistatic SAR," *IEEE Transactions on Aerospace and Electronic Systems*, Vol. 40, No. 4, 1147–1159, 2004.
21. Neo, Y., F. Wong, and I. Cumming, "A two-dimensional spectrum for bistatic SAR processing using series reversion," *IEEE Trans. Geosci. Remote Sens. Lett.*, Vol. 4, No. 2, 307–311, 2007.
22. Geng, X., H. Yan, and Y. Wang, "A two-dimensional spectrum model for general bistatic SAR," *IEEE Trans. Geosci. Remote Sens.*, Vol. 46, No. 8, 2216–2223, 2008.
23. Bamler, R., "A systematic comparison of SAR focusing algorithms," *Proc. of IGARSS '91*, 1005–1009, 1991.
24. Chang, C. Y., M. Y. Jin, and J. C. Curlander, "SAR processing based on the exact two-dimentional transfer function," *Proc. of IGARSS '92*, 355–359, 1992.
25. Eldhuset, K., "Ultra high resolution spaceborne SAR processing," *IEEE Transactions on Aerospace and Electronic Systems*, Vol. 4, No. 1, 370–378, 2004.
26. Raney, R. K. and P. W. Vachon, "A phase preserving SAR processor," *Proc. of IGARSS*, 2588–2591, 1989.
27. Cumming, I. G. and F. Wong, *Digital Processing of Synthetic Aperture Radar*, Artech House, Norwood, MA, 2005.